



# Effects of density-affecting scalar on the onset of chaos in a simplified model of thermal convection: a nonlinear dynamical perspective

Sungju Moon<sup>1</sup> , Jong-Jin Baik<sup>1,a</sup> , Jaemyeong Mango Seo<sup>2</sup>, Beom-Soon Han<sup>1</sup>

<sup>1</sup> School of Earth and Environmental Sciences, Seoul National University, Seoul 08826, South Korea

<sup>2</sup> Max Planck Institute for Meteorology, Bundesstraße 53, 20146 Hamburg, Germany

Received: 16 October 2020 / Accepted: 23 December 2020

© The Author(s), under exclusive licence to Società Italiana di Fisica and Springer-Verlag GmbH Germany, part of Springer Nature 2021

**Abstract** To explore how density-affecting scalar influences the onset of chaos in a simplified model of thermal convection, we consider three versions of a physically extended Lorenz system obtained from incorporating additional physical ingredients such as rotation and density-affecting scalar. The three versions of the extended Lorenz system correspond to the cases when the density-affecting scalar has positive, neutral, and negative impacts on buoyancy. In general, compared to the case when the density-affecting scalar has a positive (neutral) impact on buoyancy, the case when the density-affecting scalar has a neutral (negative) impact on buoyancy leads to a higher critical Rayleigh parameter, a sign of delayed onset of chaos. For an appropriate choice of parameters that lead to chaotic solutions in all three cases, it is shown that the chaotic attractors for the three cases can exhibit a variety of different characteristics, such as taking on the shape of the classic Lorenz attractor, sharing the phase space with stable point attractors, and taking an unusual shape that is distinguished from the Lorenz attractor. The different characteristics in chaotic attractors lead to qualitative differences in the behaviour exhibited by the corresponding flow and temperature patterns reconstructed from the numerical solutions. Further analysis of this simplified model offering a nonlinear dynamical perspective on the thermal convection problem is expected to serve as an avenue for gaining new insights into this and related problems.

## 1 Introduction

The Lorenz system consisting of three ordinary differential equations (ODEs) was originally derived as a simplified nonlinear model of thermal convection [1,2]. It is a quintessential example of a deterministic system exhibiting sensitive dependence on initial conditions, considered to be one of the fundamental properties of turbulence [3]. Owing to the qualitative similarities linking chaos with turbulence and other related phenomena in the lower atmosphere, many were inspired to make such connections more concrete. For example, tech-

**Electronic supplementary material** The online version of this article (<https://doi.org/10.1140/epjp/s13360-020-01047-7>) contains supplementary material, which is available to authorized users.

<sup>a</sup> e-mail: [jjbaik@snu.ac.kr](mailto:jjbaik@snu.ac.kr) (corresponding author)

niques borrowed from nonlinear dynamics have been applied to analyse measurement data, often with the goal of identifying a hypothesized attractor for boundary-layer turbulence [4–7]. Meanwhile, more theoretically grounded approaches have led to high-dimensional extensions of the Lorenz system through additional physical ingredients in the governing equations such as a density-affecting scalar [8], rotation [9], or both [10, 11]. Beyond such additional physical ingredients relevant to geophysical fluids, there have also been studies that extend the Lorenz system to include other effects such as time delay [12], electro-convection [13], or embedded magnetic fields [14]. The expectation has been that in so doing the updated conceptual models could give more complete considerations for the physical processes involved with the dynamics of thermal convection.

In this paper, we study three versions of the “physically extended” Lorenz system of Moon et al. [11] with additional considerations for density-affecting scalar and rotation. Particular attention is paid to the different roles played by the density-affecting scalar in modulating the onset of chaos as the three versions of the extended system considered in this study correspond to the cases when the density-affecting scalar has positive, negative, and neutral impacts on buoyancy. In doing so, our goal is also to explore aspects of the extended Lorenz systems relevant to studying thermal convection from the perspective of nonlinear dynamics, paving the way for potential new insights.

## 2 The extended Lorenz systems

By including additional terms for rotation and density-affecting scalar in the governing equations describing Rayleigh–Bénard convection, Moon et al. [11] derived the following six-dimensional extension of the Lorenz system:

$$\dot{X} = \sigma(Y - X) - \sigma Le^{-1}W + sV, \quad (1a)$$

$$\dot{Y} = -XZ + r_T X - Y, \quad (1b)$$

$$\dot{Z} = XY - bZ, \quad (1c)$$

$$\dot{V} = -X - \sigma V, \quad (1d)$$

$$\dot{W} = -XU + r_C X - Le^{-1}W, \quad (1e)$$

$$\dot{U} = XW - Le^{-1}bU, \quad (1f)$$

where the dot above each variable indicates the derivative with respect to the dimensionless time  $\tau$ . The parameters  $\sigma$ ,  $r_T$ , and  $b$  are, respectively, the Prandtl number, the thermal Rayleigh parameter, and the aspect-ratio parameter from the original Lorenz system [2]. The Lewis number is defined as  $Le = \nu_T/\nu_S$ , where  $\nu_T$  and  $\nu_S$  denote the thermal diffusivity and the scalar diffusivity, respectively. The rotational parameter  $s$  is given so that it is proportional to the Taylor number. The precise mathematical expressions for these parameters, developed in the context of the derivation of Eqs. (1a)–(1f), are found in Moon et al. [11]. The scalar Rayleigh parameter  $r_C$ , defined analogously to the thermal Rayleigh parameter but for scalar concentration, requires further explanation.

In the context of Rayleigh–Bénard convection, the thermal Rayleigh parameter  $r_T$  is a normalized Rayleigh number, that is, the Rayleigh number  $Ra$  divided by the critical Rayleigh number  $Ra_c$ . We write  $Ra_S$ , the Rayleigh number for scalar concentration, similarly to  $Ra$  as follows:

$$Ra = \frac{g\alpha H^3 \Delta T}{\nu_T \nu_m} \quad \text{and} \quad Ra_S = \frac{g\beta H^3 \Delta S}{\nu_S \nu_m}, \quad (2)$$

where  $g$  is the gravitational acceleration,  $H$  is the distance between the bottom and top boundaries,  $\Delta T$  and  $\Delta S$  are the preset temperature and scalar concentration differences between the bottom and top boundaries, respectively, and  $\nu_m$  is the kinematic viscosity. Both temperature and scalar concentration are set to be greater at the bottom so that  $\Delta T > 0$  and  $\Delta S > 0$ . The thermal expansion coefficient  $\alpha$  and the scalar concentration coefficient  $\beta$  are written in terms of temperature  $T$ , scalar concentration  $S$ , pressure  $p$ , and density  $\rho$  as follows:

$$\alpha = -\frac{1}{\rho} \left( \frac{\partial \rho}{\partial T} \right)_{p,S} \quad \text{and} \quad \beta = \frac{1}{\rho} \left( \frac{\partial \rho}{\partial S} \right)_{p,T}, \quad (3)$$

where subscripts  $p$ ,  $S$  and  $p$ ,  $T$  mean that these quantities are held constant. The coefficients  $\alpha$  and  $\beta$  appear in the buoyancy terms in the governing equation for  $w$ , the velocity in the  $z$ -direction, reproduced below [11]:

$$\frac{\partial w}{\partial t} + u \frac{\partial w}{\partial x} + w \frac{\partial w}{\partial z} = -\frac{1}{\rho_0} \frac{\partial p}{\partial z} + \nu_m \nabla^2 w + g(\alpha T' - \beta S'). \quad (4)$$

Here,  $u$  is the velocity in the  $x$ -direction,  $t$  is time,  $\rho_0$  is the reference density, and  $T'$  and  $S'$  denote the departures from the reference temperature and the reference scalar concentration, respectively.

In Moon et al. [11],  $\beta > 0$  was assumed, thereby only considering the case when the density-affecting scalar negatively affects buoyancy such as particulate matter in the air. The system consisting of (1a)–(1f) as they stand corresponds to the case when  $\beta > 0$ .

On the other hand,  $\beta < 0$  corresponds to the case when the density-affecting scalar positively affects buoyancy. This is also a feasible scenario; for example, the molecular weights of water vapour and methane are  $\sim 18.02$  and  $\sim 16.04$  g mol $^{-1}$ , respectively, lighter than the mean molecular weight of dry air at  $\sim 28.97$  g mol $^{-1}$ . In order to preserve nonnegativity of all nondimensionalized parameters, the scalar Rayleigh number  $Ra_S$  in (2) and, accordingly, the scalar Rayleigh parameter  $r_C$  for the  $\beta < 0$  case must be redefined with a minus sign. The derivation following Moon et al. [11] but with  $\beta < 0$  yields a new six-dimensional system consisting of the same equations as (1a)–(1f) except the sign of the term  $\sigma Le^{-1}W$  in (1a) is changed from  $-$  to  $+$  as follows:

$$\dot{X} = \sigma(Y - X) + \sigma Le^{-1}W + sV, \quad (5a)$$

$$\dot{Y} = -XZ + r_T X - Y, \quad (5b)$$

$$\dot{Z} = XY - bZ, \quad (5c)$$

$$\dot{V} = -X - \sigma V, \quad (5d)$$

$$\dot{W} = -XU + r_C X - Le^{-1}W, \quad (5e)$$

$$\dot{U} = XW - Le^{-1}bU. \quad (5f)$$

To the best of the authors' knowledge, this study is the first to investigate this newly derived extension of the Lorenz system consisting of the ODEs (5a)–(5f).

Lastly, if  $\beta = 0$ , the density-affecting scalar does not affect buoyancy. As a result, the term  $\sigma Le^{-1}W$  vanishes from (1a) in this case. Equations (1e) and (1f) decouple from the other equations in the system, yielding a four-dimensional extension of the Lorenz system known as the Lorenz–Stenflo system [9]. Previous attempts to investigate this system revealed elaborate bifurcation structures leading to a rich set of nonlinear dynamical behaviour [15, 16].

### 3 Bifurcation and onset of chaos in the simplified model

The existence of a critical  $r_T$  beyond which the Lorenz system exhibits chaos is well known [2, 17], which can also be thought to represent the onset of turbulence in thermal convection. Due to the stabilizing effects of rotation [18, 19], this threshold is raised when the rotational parameter  $s$  is included. Furthermore, an increase in the critical  $r_T$  upon including a density-affecting scalar with  $\beta > 0$  was reported in Moon et al. [11], although it was also reported that a very high  $r_C$  can lead to a brief resurgence of chaos.

To see the effects of a density-affecting scalar when the sign of  $\beta$  is changed, bifurcation diagrams using peak  $Z$ -values and Lyapunov exponent spectra along  $r_T$  are plotted in Fig. 1 for the three cases with the following parameters where applicable:  $\sigma = 10$ ,  $b = 8/3$ ,  $Le^{-1} = 0.1$ ,  $s = 40$ , and  $r_C = 60$ . The peak  $Z$ -values are recorded based on the numerical solutions obtained using the fourth-order Runge–Kutta method with the time resolution of  $\Delta\tau = 10^{-4}$  from the initial condition  $(X, Y, Z, \dots) = (1, 0, 0, \dots)$  near the trivial fixed point at the origin. This initial condition is chosen to detect the global (heteroclinic) bifurcation that leads to the first onset of chaos. In other words, we are looking for the critical  $r_T$ .

The peak  $Z$ -values along a line (e.g.,  $r_T \in [\sim 27.5, \sim 29.0]$  in Fig. 1c) indicate a nonchaotic (convergent or periodic) solution, whereas clusters of peak  $Z$ -values, as shown in Fig. 1c for  $r_T \gtrsim 29.1$ , indicate that the solution is chaotic. Note that the initial spin-up time of  $\tau = 200$  is applied before the peak  $Z$ -values are recorded. The lower  $r_T$  ranges with no recorded peak  $Z$ -values are, therefore, the result of the trajectories for convergent solutions having already approached the corresponding point attractor sufficiently close prior to  $\tau = 200$ . The amount of time it takes for a convergent solution to approach the point attractor sufficiently close is known to increase as  $r_T$  approaches the critical  $r_T$  from below [17], making it more likely even for convergent solutions to inadvertently record peak  $Z$ -values within the spin-up time. This explains the existence of peak  $Z$ -values even for the supposedly convergent solutions prior to the heteroclinic explosions at the critical  $r_T$  in Fig. 1a, c, e.

The critical  $r_T$  determined based on the peak  $Z$ -values are checked against those obtained from Lyapunov exponent spectra shown in the right column of Fig. 1. As for the Lyapunov exponents, having one or more positive Lyapunov exponents is indicative of a chaotic solution. The Lyapunov exponents are computed by applying the Gram–Schmidt orthonormalization method [20] on the numerical solutions obtained using the fourth-order Runge–Kutta method with  $\Delta\tau = 10^{-3}$  from 1000 randomly selected initial conditions around the trivial fixed point, so again we are detecting the first emergence of chaos through heteroclinic explosion. Despite the relatively coarse resolution of  $\Delta r_T = 0.1$ , the peak  $Z$ -values and Lyapunov exponents yield matching critical  $r_T$ .

There is clearly an increasing trend in the critical  $r_T$  as the impact of density-affecting scalar on buoyancy pivots from positive to neutral and from neutral to negative (Fig. 1):  $\sim 27.5$  for  $\beta < 0$ ,  $\sim 29.1$  for  $\beta = 0$ , and  $\sim 30.7$  for  $\beta > 0$ . It is interesting that for the  $\beta > 0$  case, there is a visible window of intermittent chaos from  $r_T \approx 29.6$  to  $r_T \approx 29.8$  prior to the onset of persistent chaos at  $r \approx 30.7$  (Fig. 1f), but even counting the starting point of intermittent chaos as the critical  $r_T$ , it is still higher than that for the  $\beta = 0$  case. The aforementioned results are as expected based on the effects of the density-affecting scalars on buoyancy in the three cases. When the density-affecting scalar helps with the onset of chaos by positively influencing buoyancy in thermal convection, it generally requires a lower critical  $r_T$  for chaos to emerge.

Occasionally, we have found parameter combinations (e.g.,  $s = 10$  and  $r_C = 20$ ) with which the critical  $r_T$  increases as we go from the case when  $\beta > 0$  to the case when  $\beta < 0$ , that is, in the opposite direction of the trend seen in Fig. 1. This is thought to be caused

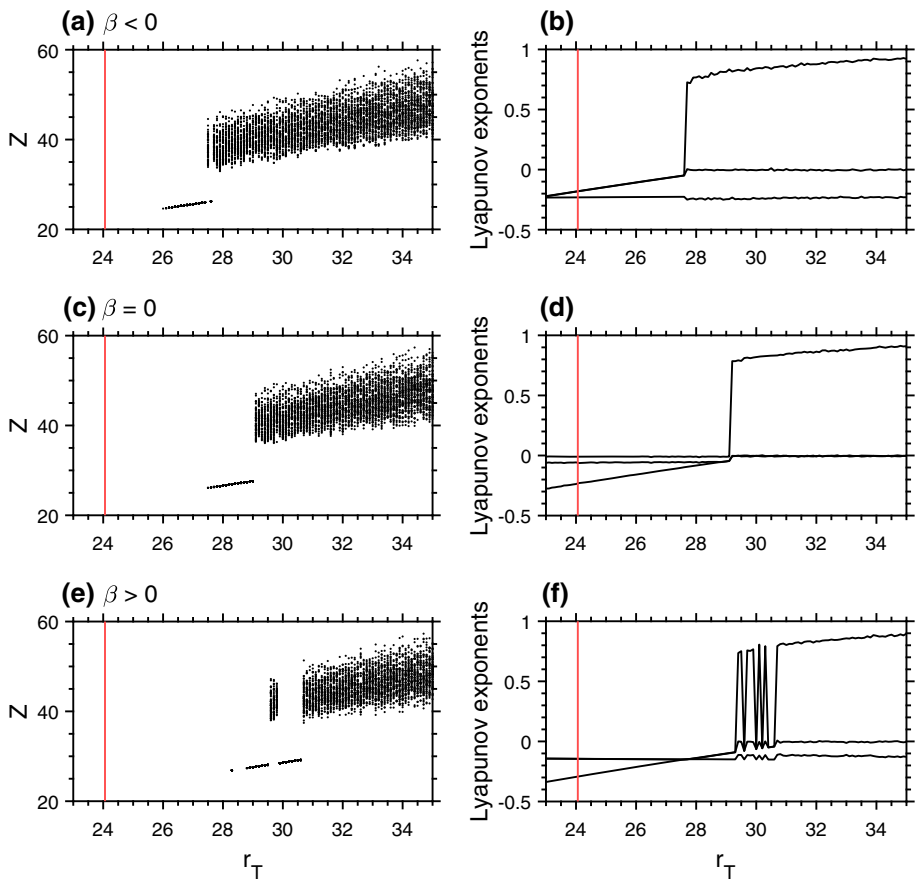


**Fig. 1** Bifurcation diagrams along the parameter  $r_T$ ,  $\Delta r_T = 0.1$ , obtained from the peak  $Z$ -values and three largest Lyapunov exponents for an extended Lorenz system with rotation and density-affecting scalar with parameters  $\sigma = 10$ ,  $b = 8/3$ ,  $Le^{-1} = 0.1$ ,  $s = 40$ , and  $r_C = 60$  where applicable for the case when **a–b**  $\beta < 0$ , **c–d**  $\beta = 0$ , and **e–f**  $\beta > 0$ . The critical  $r_T = 24.06$  for the three-dimensional Lorenz system is indicated by the red vertical lines

by a phenomenon known as attractor coexistence. A common cause of attractor coexistence in a nonlinear system is the mismatched bifurcation structure inherent to the system. When  $r_T > 1$ , the Lorenz system possesses two other nontrivial fixed points  $\mathbf{X}_h^\pm = (X, Y, Z) = (\pm\sqrt{b(r_T - 1)}, \pm\sqrt{b(r_T - 1)}, r_T - 1)$ , which are known to undergo local (Hopf) bifurcations at  $r_T \approx 24.74$  given the otherwise traditional parameter choices of  $\sigma = 10$  and  $b = 8/3$  [17]. Prior to the Hopf bifurcations,  $\mathbf{X}_h^\pm$  act as point attractors. As  $r_T$  is raised, chaotic solutions first emerge from initial conditions outside of the basins of attraction for these point attractors at  $r_T \sim 24.06$ , which leads to a brief coexistence of chaotic and non-chaotic attractors for  $r_T$  up to  $\sim 24.74$  [17, 21]. In such situations, solutions of the Lorenz system can either be chaotic or convergent depending on the initial condition. As  $r_T$  is further raised beyond  $\sim 24.74$ , Hopf bifurcations of  $\mathbf{X}_h^\pm$  lead to chaotic solutions from all initial conditions in the state space except for the fixed points and their stable manifolds. Note that changing the parameter  $b$  can also lead to different kinds of attractor coexistence such as that of two separated chaotic

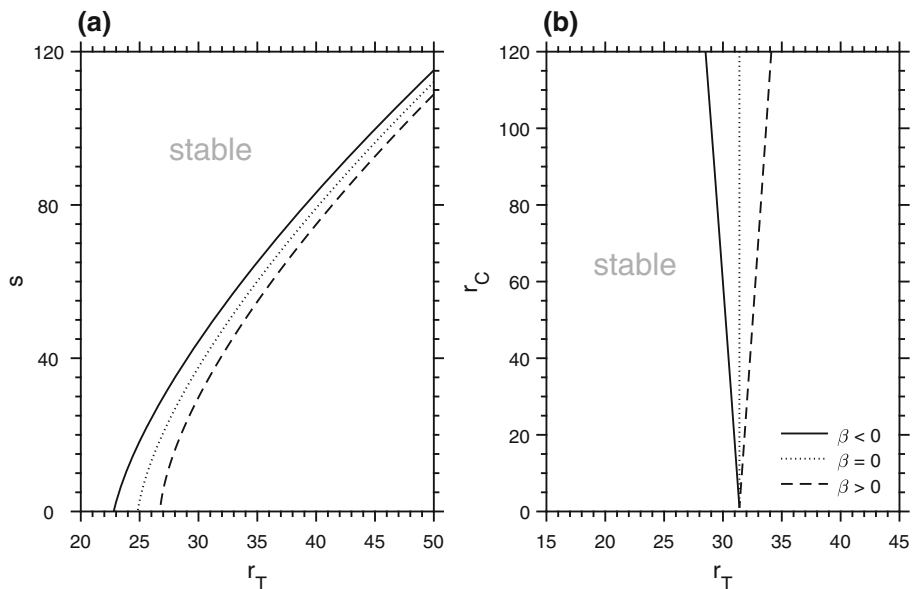


**Fig. 2** Neutral stability curves marking the local stability changes around  $\mathbf{X}_h^\pm$  for the three cases  $\beta < 0$ ,  $\beta = 0$ , and  $\beta > 0$  in **a** the  $r_T$ - $s$  space with  $r_C = 60$  and **b** the  $r_T$ - $r_C$  space with  $s = 40$

attractors around the nontrivial fixed points (*i.e.*, a “broken butterfly”) [22], but we have kept the traditional  $b = 8/3$  in this study.

All three extended Lorenz systems contain the Lorenz system as a subsystem and, therefore, inherit the two nontrivial fixed points  $\mathbf{X}_h^\pm$  that experience Hopf bifurcations from the original Lorenz system. Figure 2 shows stability curves marking Hopf bifurcations at the nontrivial fixed points  $\mathbf{X}_h^\pm$  in the  $r_T$ - $s$  and  $r_T$ - $r_C$  parameter spaces, computed based on the eigenvalues of the linearized systems around the nontrivial fixed points  $\mathbf{X}_h^\pm$  for each case. Crossing each curve from the left to right by raising  $r_T$  leads to the onset of chaos even for initial conditions near  $\mathbf{X}_h^\pm$ . That the stability curves for  $\beta > 0$  are placed to the right of those for  $\beta = 0$ , which are themselves further to the right of those for  $\beta < 0$ , suggests that the critical  $r_T$  should generally become higher as the effect of density-affecting scalar on buoyancy pivots from positive to negative; in other words, it becomes harder for chaotic motions to appear.

The rotational parameter  $s$  controls where on the  $r_T$ -axis the three curves converge in the  $r_T$ - $r_C$  space as  $r_C \rightarrow 0$  which is  $\sim 31.5$  in Fig. 2b for when  $s = 40$ . A smaller  $s$  implies a weaker rotational effect, a decrease in the critical  $r_T$ , and a leftward shifting of the convergence point. It is also noted that the gaps between the stability curves become wider as  $s$  gets smaller (Fig. 2a). Accordingly, the two kinds of density-affecting scalar would show a greater difference in their responses to an increase in  $r_C$  if  $s$  gets smaller.

The slope of the stability curves in the  $r_T$ - $r_C$  space can be linked more directly to the Lewis number  $Le$ . Denote the critical thermal and scalar Rayleigh parameters by  $r_T^c$  and  $r_C^c$ , respectively. It follows from (2) that  $|\partial r_C^c / \partial r_T^c| \approx |\partial Ra_S / \partial Ra| \approx |\beta \nu_T \Delta S / (\alpha \nu_S \Delta T)| \propto Le$ . In fact, eddy-perspective diffusivities for heat and scalar can have a similar order of magnitude in a boundary layer [23], in which case the stability curves would have flatter slopes than

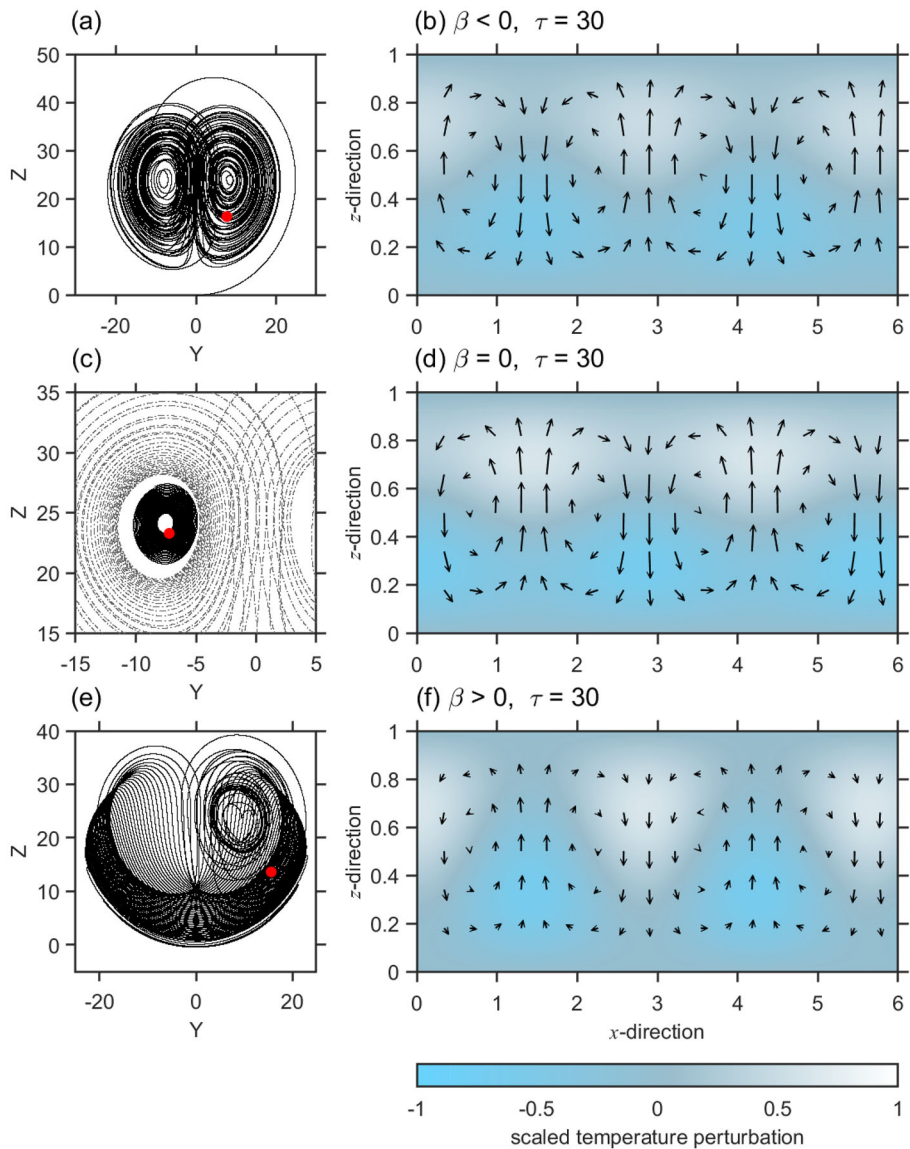


**Fig. 3** Trajectories of the numerical solutions of the extended Lorenz system corresponding to the case when **a**  $\beta < 0$  from the initial condition  $(X, Y, Z, V, W, U) = (1, 0, 0, 0, 0, 0)$ , **c**  $\beta = 0$  from the initial conditions  $(X, Y, Z, V) = (-15, -10, 24, -1)$  (solid) and  $(X, Y, Z, V) = (1, 0, 0, 0)$  (dash-dotted), and **e**  $\beta > 0$  from the initial condition  $(X, Y, Z, V, W, U) = (1, 0, 0, 0, 0, 0)$ . Scaled and nondimensionalized flow (arrows) and temperature (filled contours) at  $\tau = 30$  recovered from the solutions for the case when **b**  $\beta < 0$ , **d**  $\beta = 0$ , and **f**  $\beta > 0$ . Points in the Y-Z spaces corresponding to the specified solution states for **b**, **d**, and **f** are indicated by red dots in **a**, **c**, and **e**, respectively. The lengths in the x- and z-directions are also scaled



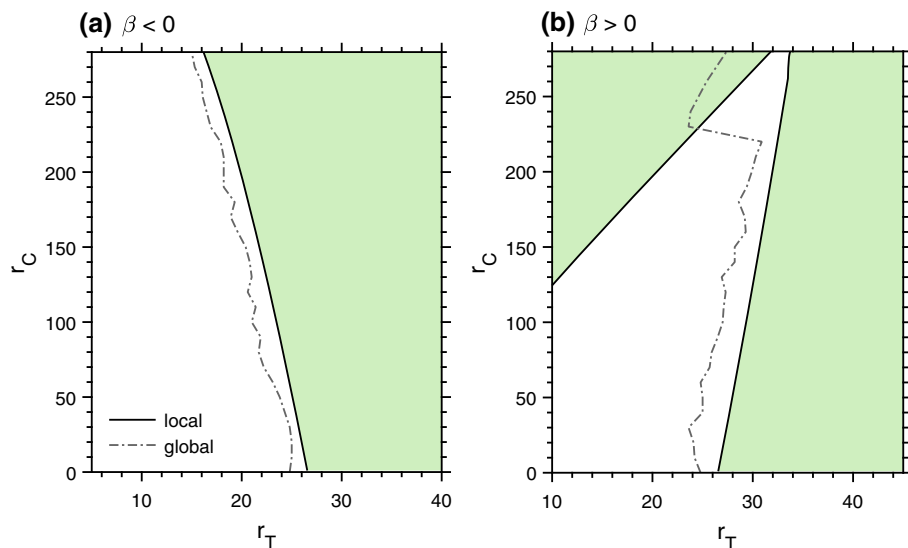


**Fig. 4** Neutral stability curves in the  $r_T$ - $r_C$  space marking the local stability changes of  $\mathbf{X}_h^\pm$  under Hopf bifurcation (solid) and global bifurcations that lead to onset of chaos as  $r_T$  is raised (dash-dotted) for the case when **a**  $\beta < 0$  and **b**  $\beta > 0$  with other parameters the same as in Fig. 3. The shaded areas indicate where  $\mathbf{X}_h^\pm$  are locally unstable

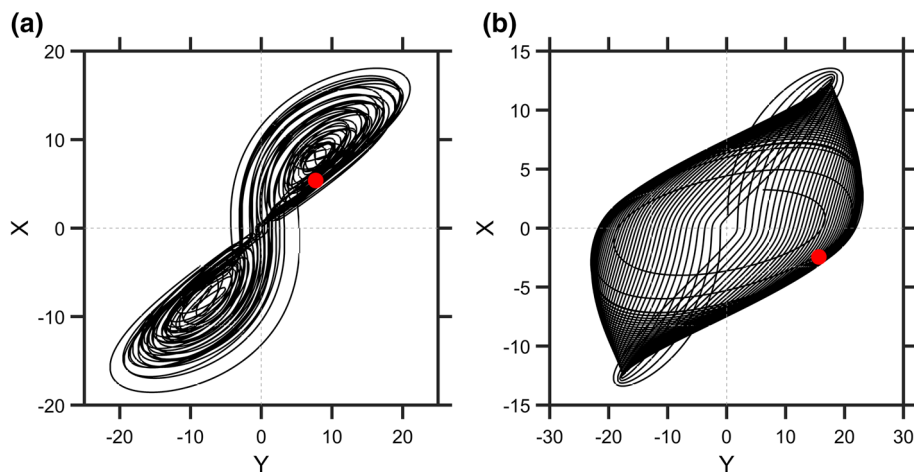


**Fig. 5** Trajectories corresponding to **a** the Lorenz-type attractor from Fig. 3a and **b** the second-onset attractor from Fig. 3e projected on the  $Y$ - $X$  plane. The red dots indicate where the particular solutions at  $\tau = 30$  corresponding to Fig. 3b, f are located

those in Fig. 2b with  $Le^{-1} = 0.1$ , leading to an even greater gap between the  $\beta < 0$  and  $\beta > 0$  cases.



#### 4 Chaotic attractors and associated flow patterns

In this section, a particular combination of parameter values is chosen to examine the three versions of the extended Lorenz system for their chaotic attractors and the associated flow and temperature patterns reconstructed from the numerical solutions as shown in Fig. 3. Given the parameter combination,  $\sigma = 10$ ,  $r_T = 25$ ,  $b = 8/3$ ,  $Le^{-1} = 0.1$ ,  $s = 10$ , and  $r_C = 250$ , the  $\beta > 0$  case is expected to exhibit the so-called second-onset of chaos, a brief resurgence of chaos when  $r_C$  is very high before stabilizing ultimately as  $r_C$  is further raised [11]. Indeed, the system corresponding to the case when  $\beta > 0$  exhibits a chaotic attractor (Fig. 3e) that is qualitatively distinct from the Lorenz attractor, hereafter referred to as the second-onset attractor. On the other hand, the numerical solution for the  $\beta < 0$  case embodies a chaotic trajectory typically found in association with the Lorenz attractor (Fig. 3a). Therefore, this attractor is said to be Lorenz-type. Interestingly, the Lorenz–Stenflo system for the  $\beta = 0$  case features coexistence of chaotic and point attractors (Fig. 3c), while the other cases do not exhibit any such coexistence. This can be understood by examining the underlying bifurcation structures discussed below.

The kind of coexistence shown in Fig. 3c is caused by the mismatches in local bifurcations of the nontrivial fixed points and the global bifurcation that leads to the first emergence of chaos. Accordingly, in Fig. 4, we compare the neutral stability curves marking both kinds of bifurcations in the  $r_T$ – $r_C$  space. The neutral stability curves for local bifurcations are computed based on the same linear stability analysis method used for Fig. 2. To plot the global bifurcation curves in Fig. 4, the critical  $r_T$  for each fixed  $r_C$  is determined by brute-force checking of the solution types while raising  $r_T$  using the numerical solutions from the initial condition  $(X, Y, Z, V, W, U) = (1, 0, 0, 0, 0, 0)$  with the resolutions  $\Delta r_C = 10$  and  $\Delta r_T = 0.1$ .

The  $r_T$ -intercepts of the neutral stability curves show a narrow gap between the global ( $r_T \sim 24.8$ ) and local ( $r_T \sim 26.5$ ) bifurcations, resulting in the coexistence of chaotic and convergent attractors there. Since the stability curve for the  $\beta = 0$  case does not depend on  $r_C$  (Fig. 2b), we can expect this coexistence to persist even as  $r_C$  is further raised as shown in Fig. 3c at  $r_C = 250$ . On the other hand, the stability curves are leftward-tilted for the  $\beta < 0$  case (Fig. 4a) in alignment with the expected effects of the density-affecting scalar with a positive impact on buoyancy. At high  $r_C$ , therefore, the kind of coexistence seen in Fig. 3c requires lower  $r_T$  values in this case, which explains why no such coexistence is seen in Fig. 3a.

The bifurcation structure is more complicated for the case when  $\beta > 0$  because now the stabilizing effects of the density-affecting scalar competes against the destabilizing effects of raising  $r_T$ . In addition to the expected region of the  $r_T$ – $r_C$  plane where the nontrivial fixed points are locally unstable to the right of the positively sloped neutral stability curve intercepting the  $r_T$ -axis at  $\sim 26.5$  (first local stability curve), there is another region of local instability to the left of the second local stability curve, which is visible for  $r_C \gtrsim 124$  in Fig. 4b. It appears that at high-enough  $r_C$ , the tug-of-war between the two competing effects of intensifying the density-affecting scalar and raising the thermal Rayleigh parameter leads to another locally unstable regime. The global bifurcation curve marking the first onset of chaos initially follows the rightward-tilting direction of the first local stability curve as  $r_C$  is raised, but it then jumps to the left of the second local stability curve between  $r_C = 220$  and  $r_C = 230$ . As a result, given the parameter values, the  $\beta > 0$  case narrowly misses the potential region for attractor coexistence, and there thus remains only a chaotic attractor as shown in Fig. 3e. This difference in the bifurcation structure at high  $r_C$  can be the reason

why the resultant attractor (Fig. 3e) for the  $\beta > 0$  case is shaped quite differently from the classic Lorenz-type attractor (Fig. 3a).

To see how these qualitative differences in the chaotic attractors manifest in the simplified model of convection, the flow and temperature patterns are reconstructed from the numerical solutions of the ODE systems. The snapshots are shown in Fig. 3b, d, f each corresponding to the position of the solution state (red dot) along the trajectory shown to its left. The trajectories belonging to the Lorenz attractor are known to unpredictably alternate between two chaotic regimes corresponding to the “wings” of the butterfly-shaped attractor [24]. The flow pattern and convective cells in Fig. 3b are associated with the right-hand-side wing of the attractor shown in Fig. 3a, where  $Y$  is positive. Corresponding to the left-hand-side wing are the flow pattern and convective cells resembling those in Fig. 3d. The case when  $\beta < 0$  with the same parameter values, therefore, exhibits regime changes between the patterns of Fig. 3b and d. The details of this transition between the flow regimes can be seen in the first part of the supplementary animation (Online Resource 1).

Similarly, the flow patterns for the case when  $\beta = 0$  reconstructed from chaotic solutions with initial conditions near the trivial fixed point would feature intermittent regime changes in the flow and temperature patterns (not shown). Sharing the phase space with the chaotic attractor are two stable point attractors near the nontrivial fixed points, one of which is shown in Fig. 3c (solid). As the trajectory of this convergent solution spirals inward toward the point attractor at the nontrivial fixed point, the flow pattern associated with the left-hand-side wing of the Lorenz attractor is maintained, and the layer of hot pockets continues to pile up (Fig. 3d). This suggests that, for some initial conditions, the switching back-and-forth between the two regimes ceases in the absence of density-affecting scalar (*i.e.*, going from  $\beta < 0$  or  $\beta > 0$  to  $\beta = 0$ ), resulting in a stationary convective structure.

Note that the flow regime itself depends more directly on the sign of variable  $X$  rather than that of variable  $Y$ . In the derivation, the series expansion of the stream function  $\psi$  that determines the flow in this simplified model via  $u = -\partial\psi/\partial z$  and  $w = \partial\psi/\partial x$  is truncated to the first mode as follows:

$$\psi = C_1 X(t) \sin(k_x x) \sin(k_z z), \quad (6)$$

where  $C_1$  is a constant coefficient and  $k_x$  and  $k_z$  are the scales for wavenumbers in the  $x$ - and  $z$ -directions, respectively [2, 11]. The reason why the regime transitions appear to follow the changes in the sign of  $Y$  in the Lorenz attractor is because the sign of  $X$ , for the most part, coincides with that of  $Y$  in the trajectories representing the Lorenz attractor. Figure 5a shows the  $Y$ - $X$  projection of the trajectory in Fig. 3a, revealing the figure 8-shaped twists in the trajectories around  $(X, Y) = (0, 0)$  causing  $X$  and  $Y$  to share the sign within the first and third quadrants when projected on the  $Y$ - $X$  plane.

In contrast, different transition patterns emerge from the solutions for the case when  $\beta > 0$  (Fig. 3f) owing to the differently shaped chaotic trajectory (Fig. 3e) representing the second-onset attractor. Whereas in the  $\beta < 0$  case the flow regime transition depends on the position of the solution state along the chaotic trajectory, the regime transition in the  $\beta > 0$  case now depends on the direction in which the trajectory is headed. The flow pattern resembles that shown in Fig. 3f (downward at the center of the plot) when the solution state moves from the right-hand-side ( $Y > 0$ ) to the left-hand-side ( $Y < 0$ ) along the trajectory, and an opposite pattern (upward at the center of the plot) arises when the solution state moves from the left-hand-side to the right-hand-side of Fig. 3e. Further details in the regime transitions associated with the second-onset attractor are shown in the second part of the supplementary animation (Online Resource 1). The difference is caused by the differently shaped attractors in these two cases. The  $Y$ - $X$  projection of the trajectory in Fig. 5b shows that, except around the two

extrema in the first and third quadrants of the  $Y$ - $X$  projection, the trajectory continuously traces shapes that resemble a rhomboid with rounded corners. The solution state traverses along the trajectory clockwise so that as it switches from  $Y < 0$  to  $Y > 0$ ,  $X$  remains positive for the most part (upper half of Fig. 5b), and as it switches from  $Y > 0$  to  $Y < 0$ ,  $X$  remains mostly negative (lower half of Fig. 5b).

Another difference between the two cases lies in the manner in which the regime changes occur. Under the Lorenz attractor, the solution state intermittently switch between the two wings, appearing to prefer one regime over another at times, despite the symmetry inherent to the Lorenz attractor [25]. On the other hand, regime changes are initially more frequent and almost regular under the second-onset attractor. As a result, unlike the temperature patterns shown in Fig. 3b, d, the rising hot pockets in Fig. 3f are not given much chance to spread out in the  $x$ -direction once they reach the top. Only in longer-term solutions (*e.g.*,  $\tau \gtrsim 300$ ) does it prominently develop such a preference of one regime over another resulting from the occasional intermittency in the regime transitions. In the long-run, both the trajectories for the Lorenz and the second-onset attractors should eventually reveal the symmetry inherent to these systems, but a much longer integration time is expected before the symmetry takes shape under the second-onset attractor [11].

## 5 Conclusions

The three versions of the physically extended Lorenz system were obtained by including rotation and density-affecting scalar endowed with different impacts on buoyancy. By also considering the case when the density-affecting scalar positively affects buoyancy, this study is an extension of previous studies such as Veronis [8] and Moon et al. [11] in which the density-affecting scalar only negatively affects buoyancy or Stenflo [9] in which the density-affecting scalar has no effect on buoyancy. By examining the bifurcation structures and stability around the nontrivial fixed points, it was confirmed that depending on whether the density-affecting scalar has positive, neutral, or negative impacts on buoyancy, the onset of chaos via raising the Rayleigh parameter generally becomes easier, unchanged, or more difficult, respectively. Furthermore, the reconstructed flow and temperature patterns demonstrate different scenarios possible as chaos emerges in these systems: intermittent switching between two regimes under a Lorenz-type attractor, coexistence of chaotic and stagnant behaviour, and an unusually shaped attractor with distinct characteristics when compared to the Lorenz attractor. It is notable that while the difference between the  $\beta < 0$  and  $\beta > 0$  cases manifests only through the flipped sign of a single term in the equations, this small change in the equations can still bring about fundamentally altered behaviour.

The above results highlight how at a fundamental level these simplified models are able to distil the nonlinear behaviour inherent to thermal convection. Incorporating additional physical ingredients in this way brings the conceptual model of Lorenz closer to the physical reality while preserving still the core dynamical features of the Lorenz system. Indeed, all three systems considered here contain the original Lorenz system as a subsystem, enabling comparisons based on the shared criteria such as the threshold parameter values for the onset of chaos, fixed points and their stability conditions, and the idiosyncratic behaviour of the solution trajectories when they are chaotic. Further analysis of these extensions of the Lorenz system may lead to novel intuitions about the long-debated problem of identifying the hypothesized hard limit on atmospheric predictability [26]. In addition, other aspects of the extended Lorenz systems that are not fully explored in this study including chaos

synchronization [27] deserve further investigation for their potential utility in related areas of study such as the rapidly progressing field of data assimilation.

It is noted that the inclusion of additional physical ingredients still does not resolve the problems arising from the severe truncation of the Fourier expansions appearing in the derivation of the Lorenz system. Several attempts have been made to shed light on this issue by extending the Lorenz and Lorenz-like systems to higher dimensions via the inclusion of additional Fourier modes [28, 29], but still more thorough analyses are needed to clarify precisely what aspects of reality are lost during the truncation processes. A future study focusing on higher-dimensional extensions of the six-dimensional system may help such endeavours.

**Acknowledgements** The authors are grateful to two anonymous reviewers for their helpful comments and suggestions.

**Data Availability Statement** The datasets generated during and/or analysed during the current study are available from the corresponding author on reasonable request.

## Declarations

**Funding** This work was supported by the Small Grant for Exploratory Research (SGER) program through the National Research Foundation of Korea (NRF-2018R1D1A1A02086007).

**Conflict of interest** The authors have no conflicts of interest to declare that are relevant to the content of this article.

**Code availability** The MATLAB and Fortran custom codes used in this study are available from the corresponding author upon request.

## References

1. B. Saltzman, J. Atmos. Sci. **19**, 329–341 (1962)
2. E.N. Lorenz, J. Atmos. Sci. **20**, 130–141 (1963)
3. J.C. Wyngaard, *Turbulence in the Atmosphere* (Cambridge University Press, Cambridge, 2010)
4. E. Yee, Boundary-Layer Meteorol. **57**, 49–78 (1991)
5. G. Poveda-Jaramillo, C.E. Puente, Boundary-Layer Meteorol. **64**, 175–197 (1993)
6. R.O. Weber, P. Talkner, G. Stefanicki, L. Arvisais, Boundary-Layer Meteorol. **73**, 1–14 (1995)
7. M.C. Gallego, J.A. García, M.L. Cancillo, Boundary-Layer Meteorol. **100**, 375–392 (2001)
8. G. Veronis, J. Fluid Mech. **34**, 315–336 (1968)
9. L. Stenflo, Phys. Scripta **53**, 83–84 (1996)
10. L.R.M. Maas, Tellus **46A**, 671–680 (1994)
11. S. Moon, J.M. Seo, B.-S. Han, J. Park, J.-J. Baik, Chaos **29**, 063129 (2019)
12. G.M. Mahmoud, A.A. Arafa, E.E. Mahmoud, Eur. Phys. J. Plus **132**, 461 (2017)
13. P.G. Siddheshwar, D. Uma, B. Shivaraj, Eur. Phys. J. Plus **135**, 138 (2020)
14. W.M. Macek, Nonlinear Dyn. **94**, 2957–2968 (2018)
15. M.Y. Yu, Phys. Scripta **T82**, 10–11 (1999)
16. P.C. Rech, Phys. Scripta **91**, 075201 (2016)
17. J.A. Yorke, E.D. Yorke, J. Stat. Phys. **21**, 263–277 (1979)
18. S. Chandrasekhar, Proc. R. Soc. Lond. **217**, 306–327 (1952)
19. A. Prosperetti, Phys. Fluids **24**, 114101 (2012)
20. F. Christiansen, H.H. Rugb, Nonlinearity **10**, 1063–1072 (1997)
21. C. Sparrow, *The Lorenz Equations: Bifurcations, Chaos, and Strange Attractors* (Springer, New York, 1982)
22. C. Li, J.C. Sprott, Int. J. Bifurc. Chaos **24**, 1450131 (2014)
23. A.A.M. Holtslag, C.-H. Moeng, J. Atmos. Sci. **48**, 1690–1698 (1991)
24. T.N. Palmer, Bull. Am. Meteorol. Soc. **74**, 065202 (1993)
25. E.J. Doedel, B. Krauskopf, H.M. Osinga, Nonlinearity **19**, 2947–2972 (2006)

26. F. Zhang, Y.Q. Sun, L. Magnusson, R. Buizza, S.-J. Lin, J.-H. Chen, K. Emanuel, *J. Atmos. Sci.* **76**, 1077–1091 (2019)
27. G.S. Duane, J.J. Tribbia, J.B. Weiss, *Nonlinear Process. Geophys.* **13**, 601–612 (2006)
28. B.-W. Shen, *J. Atmos. Sci.* **71**, 1701–1723 (2014)
29. J. Park, B.-S. Han, H. Lee, Y.-L. Jeon, J.-J. Baik, *Phys. Scripta* **91**, 49–65 (2016)